remote sensing

MDPI

Article

Assessment of Atmospheric Correction Algorithms for Sentinel-3 OLCI in the Amazon River Continuum

Aline M. Valerio [1,2,*], Milton Kampel [1], Vincent Vantrepotte [3,4], Victoria Ballester [2] and Jeffrey Richey [5]

[1] Monitoring Oceans from Space Laboratory, Earth Observation and Geoinformatics Division, National Institute for Space Research (INPE), São José dos Campos 12227-010, SP, Brazil; milton.kampel@inpe.br
[2] Center for Nuclear Energy in Agriculture, São Paulo University (CENA-USP), Piracicaba 13400-970, SP, Brazil; vicky@cena.usp.br
[3] Institut de Recherche et Développement (IRD), Centre National de la Recherche Scientifique (CNRS), Université Lille, Université Littoral Côte d'Opale (ULCO), UMR 8187, Laboratoire d'Océanologie et de Géosciences (LOG), 59000 32 Avenue Foch, 62930 Wimereux, France; vincent.vantrepotte@univ-littoral.fr
[4] Tropical Atlantic Interdisciplinary Laboratory on Physical, Biogeochemical, Ecological and Human Dynamics (IJL TAPIOCA), Departamento de Oceanografia, Universidade Federal de Pernambuco, Avenida Arquitetura, S/N, Recife 50670-901, PE, Brazil
[5] School of Oceanography, University of Washington (UW), Seattle, WA 98195, USA; jrichey@uw.edu
* Correspondence: aline.valerio@inpe.br; Tel.: +55-(12)-3208-6454

Abstract: Water colour remote sensing is a valuable tool for assessing bio-optical and biogeochemical parameters across the vast extent of the Amazon River Continuum (ARC). However, accurate retrieval depends on selecting the best atmospheric correction (AC). Four AC processors (Acolite, Polymer, C2RCC, OC-SMART) were evaluated against in situ remote sensing reflectance (R_{rs}) measurements. K-means classification identified four optical water types (OWTs) that are affected by the ARC. Two OWTs showed seasonal differences in the Lower Amazon River, influenced by the increase in suspended sediment concentration with river discharge. The other OWTs in the Amazon River Plume are dominated by phytoplankton or by a mixture of optically significant constituents. The Quality Water Index Polynomial method used to assess the quality of in situ and orbital R_{rs} had a high failure rate when the Apparent Visible Wavelength was >580 nm for in situ R_{rs}. OC-SMART R_{rs} products showed better spectral quality compared to R_{rs} derived from other AC processors evaluated in this study. These results improve our understanding of remotely sensing very turbid waters, such as those in the Amazon River Continuum.

Keywords: atmospheric correction; Amazon River Continuum; turbid waters; optical water types; spectral quality

Citation: Valerio, A.M.; Kampel, M.; Vantrepotte, V.; Ballester, V.; Richey, J. Assessment of Atmospheric Correction Algorithms for Sentinel-3 OLCI in the Amazon River Continuum. *Remote Sens.* **2024**, *16*, 2663. https://doi.org/10.3390/rs16142663

Academic Editors: Junshi Xia, Pavel Kishcha, Dar Roberts, Heidi Van Deventer and Simona Niculescu

Received: 16 May 2024
Revised: 25 June 2024
Accepted: 12 July 2024
Published: 20 July 2024

1. Introduction

Rivers and their marine receiving waters form an integrated system. The flow of the water, starting with the rainfall and headwaters, transports particulate and dissolved matter from land to sea, driving the biogeochemical cycling of a range of components throughout the river's course and continuing as it enters the ocean [1–3]. Outside the river basin limits, the river plume is an important component that integrates different water masses. Freshwater river plumes have a significant impact on the salinity, sea surface temperature, nutrients, carbon availability and primary production [4–12]. Understanding the biogeochemical dynamics induced by the land–ocean exchange is, therefore, crucial.

The Amazon River Continuum (ARC), from the lower tidal river at Óbidos 850 km to the estuary and out into the plume, is a particularly challenging environment to understand due to its sheer size, diversity of water types from low to high colour range, and tidal to seasonal cycles. In situ sampling, while fundamental, poses a significant challenge to the establishment of an effective and representative monitoring scheme, given the large

distances between sampling stations and the usual temporal nature of sampling [13,14]. With its ability to assess large areas, water colour remote sensing (WCRS) provides a critical capability to augment point measurements. For accurate retrieval of remote sensing reflectance (R_{rs}) and bio-optical properties by WCRS to assess the biogeochemical dynamics of a given area, a reliable atmospheric correction (AC) is essential.

The high turbidity of the ARC can add complexity to AC performance compared to other optically complex waters. Elevated suspended sediment concentrations show a strong signal response in the near-infrared spectrum, potentially leading to the misclassification of water pixels as clouds and an overestimation of aerosols [15]. This can result in misleading WCRS products, such as negative reflectance values [16] when processing satellite data with open ocean colour as the default setting in the AC processor [17]. In addition, AC for blue wavelengths is often challenging, especially in turbid waters [16,18–20], and can lead to problems with chlorophyll-*a* concentration (chla) retrieval, such as overestimation [17,21,22].

The ARC is also known for the high presence of coloured dissolved organic matter (CDOM) [23], which enhances water absorption, particularly in the blue-green part of the spectrum, thereby reducing the signal of water leaving radiance. The significant presence of CDOM, resulting in a low radiometric signal, has a direct impact on the signal-to-noise ratio, requiring precise (e.g., high spectral resolution) remotely sensed radiometric signals that rely heavily on effective atmospheric correction [24,25].

As a step towards developing a WCRS-based characterisation of the ARC, the overall objective of this study was to evaluate different atmospheric correction algorithms applied to Sentinel 3 Ocean and Land Colour Instrument (OLCI) images and to assess the quality of the in situ and remotely sensed spectra. Standard AC algorithms are designed to perform well in open ocean waters. These algorithms typically estimate aerosol radiance by assuming negligible water leaving radiance (black pixel assumption) in the near-infrared (NIR) bands, where pure water strongly absorbs light [16,26]. NIR bands are commonly used to estimate the atmospheric contribution, which is then extrapolated to the visible bands. However, in turbid waters, the retrieval of water leaving reflectance is hampered by increased light backscattering from suspended particles. This results in the water leaving signal becoming significant in the NIR bands. Therefore, for accurate atmospheric correction, it is essential to distinguish between aerosol and water leaving contributions at the top of the atmosphere. In turbid waters where the NIR-based black pixel assumption is no longer valid [16,20], atmospheric correction algorithms based on the short-wave infrared (SWIR) region can provide a viable solution [16,21].

There are few studies in the ARC that evaluate the performance of existing AC algorithms for the Amazon River and floodplains. However, these studies are limited to Sentinel 2 MultiSpectral Instrument (MSI) [27–29] and/or Landsat 8 Operational Land Imager (OLI) [27,28]. Although the S3-OLCI is a medium spatial resolution sensor (300 m), it can be used to assess the water colour of the Amazon River [23] and has the advantage of a better spectral resolution than the previously mentioned sensors. Recently, this sensor has been used to assess the performance of AC processors in the optically complex coastal waters of French Guiana [30], a region seasonally influenced by the ARC due to its geographical proximity.

To achieve optimal accuracy in WCRS products, it is essential to assess the data quality of both in situ and satellite R_{rs}. The Quality Water Index Polynomial (QWIP) is an effective tool for this purpose. The QWIP score helps to diagnose outliers and subtle problems with the R_{rs} data by identifying spectra that deviate significantly from expected shapes. This technique provides a quick visual tool for assessing spectral shape and magnitude, making it useful for a wide range of assessments of aquatic water-leaving reflectance spectra [31]. Furthermore, as shown in [32], QWIP has the potential to evaluate the performance of different AC approaches. Therefore, this study assesses the quality of in situ and remotely sensed spectra obtained in the region and evaluates four different

atmospheric correction algorithms applied to S3-OLCI images in the Amazon River Continuum.

2. Materials and Methods

2.1. Study Area: Lower Amazon River to the Amazon Plume

The Amazon River Continuum considered in this study extends from the upstream boundary at Óbidos (01°55.14′S, 55°31.54′W) to the Amazon River Plume (Figure 1). The region from Óbidos to the estuary is characterised by extensive floodplains and a main river channel that becomes wider and slower toward the estuary [33]. The lower part of the reach is divided around the island of Marajó, where tides of ~3 m (detectable as far as Óbidos) create semi-diurnal flows to and from floodplains and channels, resulting in complete flow reversal (but no salinity intrusion). As summarised by [34], the Amazon River plume is transported up to 1000 km away from the coast by four main water export pathways [9,35]. Amazon River discharge peaks in spring (April–May) during the northward migration of the Intertropical Convergence Zone (ITCZ), when onshore winds are relaxed. In the following summer (June–July), river discharge begins to feed the North Equatorial Counter Current (NECC), and in September, plume water is exported eastward through this pathway [36].

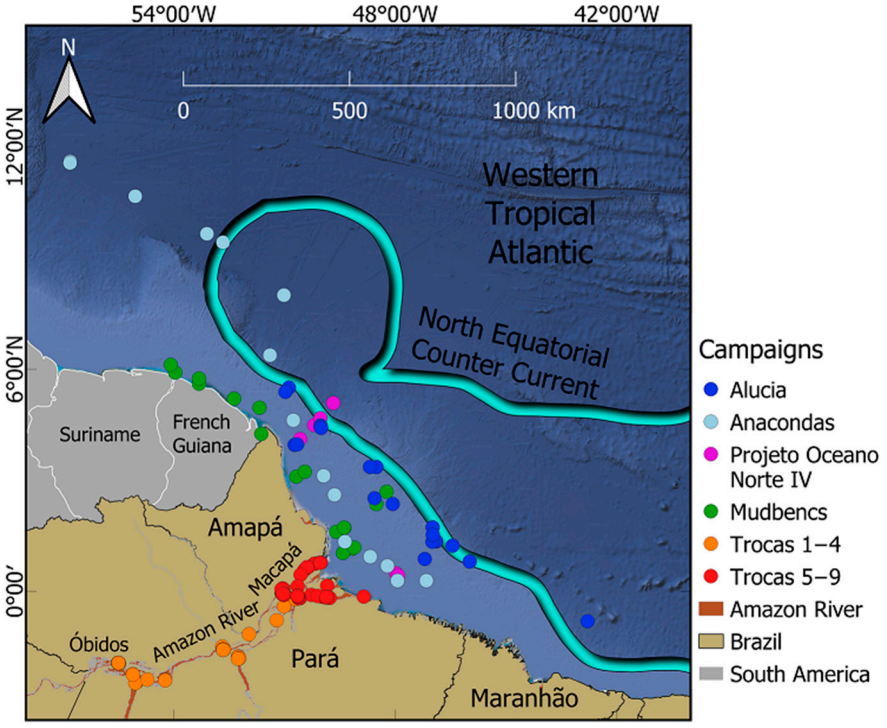

Figure 1. Sampling stations along the Amazon River Continuum used in this study. Each campaign has a different colour (see Table 1).

Table 1. Campaigns gathered in the Amazon River Continuum.

Campaign	Region	Year	Number of In Situ Radiometric Data
TROCAS 1:4	Lower Amazon River	2014–2016	55
TROCAS 5:9	Amazon River mouth	2017–2023	98
Mudbencs	Amazon River plume	2023	19
Alucia	Amazon River plume	2017	28
Anacondas	Amazon River plume	2012	19
Oceano Norte IV	Amazon River plume	2009	11

Total	230

2.2. Sampling Campaigns: In Situ Data

Radiometric data were collected over the last 14 years (2009–2023), comprising a total of 428 measurements during this period. Figure 1 gives an overview of all the campaigns considered in this study, while Table 1 provides detailed information about each campaign. In brief, radiometric and chemical measurements were made during a series of nine TROCAS project expeditions over the lower Amazon. Four expeditions were carried out along the lower Amazon River between April 2014 and March 2016, during periods of low, rising, high and falling river discharge periods (Figure 1) at Óbidos, Almeirim (approximately halfway to the mouth) and two well-constrained channels by Macapá. Measurements were made during five subsequent expeditions, 2017–2023, at the two Macapá stations and two stations bracketing the estuary. Intermediate measurements were taken on all expeditions. Chemical and radiometric measurements were carried out offshore as part of the Mudbencs project. Previous measurements were made during the Anacondas, Alucia and Oceano Norte IV campaigns.

Above-water hyperspectral radiance (L, μW m^{-2} sr^{-1}) was recorded using a portable hyperspectral spectroradiometer FieldSpec® (ASD Inc., Boulder, CO, USA; 350–1100 nm). The acquisition geometry followed recommendations to minimise shadows and avoid sun glint contamination of the measurements [37]. Radiometric measurements were performed between 09:00 and 16:00 local time. Total water leaving radiance (L_w), sky radiance (L_{sky}), and the radiance from a white panel Spectralon reference (L_g) were measured 10 times in succession. L_g is used to estimate the downwelling irradiance (E_d) (Equation (1)):

$$E_d(\lambda) = L_g(\lambda) f_c \pi, \quad (1)$$

where the correction factor f_c is determined by the ratio of a standard Spectralon reference kept in the laboratory to the Spectralon panel used in the fieldwork. The remote sensing reflectance (R_{rs}) is then calculated from Equation (2):

$$R_{rs} = \frac{L_w}{E_d} = \frac{L_u - \rho_{air-water} * L_{sky}}{E_d}, \quad (2)$$

where L_u represents the upwelling radiance reaching the sensor and $\rho_{air-water}$ is the correction coefficient accounting for sky glint at the air–water interface.

2.3. Data Processing

Various methods have been proposed in the literature to correct optical signals affected by sun glint interference. In this study, two approaches were used to assess the accuracy of the results. The first approach is based on [38] and is indicated for turbid to highly turbid waters. The correction coefficient $\rho_{air-water}$ is parameterised by wind speed and cloud cover (Equations (3) and (4)).

$$\frac{L_{sky}(\lambda=750)}{E_d(\lambda=750)} \geq 0.05 \rightarrow \rho_{air-water} = 0.0256, \quad (3)$$

or

$$\frac{L_{sky}(\lambda=750)}{E_d(\lambda=750)} < 0.05 \rightarrow \rho_{air-water} = 0.0256 + 0.00039W + 0.000034W^2, \quad (4)$$

where W is the wind measured concurrently with the radiometric measurements.

The second approach is the Three-Component Reflectance Model (3C), initially designed to improve the estimation of R_{rs} using above-water radiometric hyperspectral measurements performed under sub-optimal conditions, such as cloudy skies, varying viewing geometry, high glint disturbances and low illumination conditions [39]. The in-water component of 3C is based on a semi-analytical bio-optical model that provides R_{rs}

as a function of the optical properties of the significant water constituents and various boundary conditions. For this study, we used parameter bounds and initial estimates for the 3C retrievals for measurements significantly affected by sun glint. The table with suggested parameter bounds and access to the 3C model can be found in [39]. The processing of the raw radiometric data followed the methodology proposed by [37], with the correction for sun and sky glint as recommended by [38] and the application of the 3C model.

2.4. In Situ R_{rs} Classification

2.4.1. Spectra Normalisation

The aim of the normalisation is to reduce first-order variability in reflectance and emphasise spectral shape, thereby eliminating amplitude differences due to concentration variations. Normalisation is a standard procedure prior to optical classification, as demonstrated in previous studies [23,40,41]. Each R_{rs} spectrum was normalised by its integrated value [23,40,41] according to Equation (5). Integration was performed using the trapezoidal method over the 400–800 nm spectral range.

$$r_n(\lambda) = \frac{R_{rs}(\lambda)}{\int_{\lambda_1}^{\lambda_2} R_{rs}(\lambda) d\lambda}, \quad (5)$$

where $r_n(\lambda)$ (in units of nm^{-1}) is the normalised spectrum obtained by integration between λ_1 (400 nm) and λ_2 (800 nm).

2.4.2. Optical Water Type Identification

In this study, we used an unsupervised k-means classification of the normalised in situ R_{rs} to identify the different optical water types (OWT) within the Amazon River Continuum in order to partition the responses of the respective AC processors. The use of k-means classification is well-established in water colour studies. It has been used successfully in a variety of settings, including highly turbid waters such as our study area and other river-influenced waters [23,32,41]. To determine the optical number of clusters (k) for optical classification, we employed the Silhouette width analysis [42]. The analysis was performed over a range of 2–10 clusters.

2.5. Satellite Data

A total of 56 Level 1 OLCI images from the Sentinel-3 satellites (S3A and S3B, 300 m spatial resolution) were acquired via the CREODIAS platform (https://explore.creodias.eu/, accessed on 11 July 2024) and the Copernicus Online Data Access (https://data.eumetsat.int/, accessed on 11 July 2024). The acquired images correspond to the day of the in situ measurements, as well as one day before and one day after.

For the match-up analysis between satellite and in situ data, the mean satellite-derived R_{rs} in a 3 × 3 pixel window cantered on each in situ station with more than 5 valid pixels (non-NAN) and <20% of the coefficient of variation was considered [43,44]. In addition, the match-up analysis has identified the samples that fall within and outside the 3 h satellite pass window.

2.5.1. Selected Atmospheric Correction Algorithms

Each processor was operated using the default settings, as these are generally considered to be the best options for use without prior knowledge of the aquatic system or atmospheric conditions, including the recommended water correction settings. If the atmospheric correction produced R_{rs} (sr^{-1}), this option was selected. If normalised water-leaving reflectance (ϱw, dimensionless) was produced, the output was transformed to R_{rs} by dividing by π. If the processor offered the option to obtain ancillary data by registering for an EarthData account (https://www.earthdata.nasa.gov/, accessed on 11 July 2024), this option was selected. A general overview of the selected atmospheric correction is given in Table 2.

The following atmospheric correction algorithms, designed for coastal and/or turbid waters, were considered in this study: (i) The Acolite processor was developed by the Royal Belgian Institute of Natural Sciences [45]. By default, it employs the Dark Spectrum Fitting (DSF) approach [46,47], which was used in this study. This AC scheme is entirely image-based and, as such, does not require external inputs such as aerosol optical thickness (whether measured or estimated). The algorithm operates under the assumption that the atmosphere is homogeneous across a scene or sub-scene, allowing the prediction of atmospheric path reflectance from multiple dark targets within the scene or sub-scene. The selection of these targets is based on the lowest observed Top-Of-Atmosphere (TOA) reflectance values across all bands. Acolite offers flexibility, as it can also be configured using SWIR bands [21,45] by setting the aerosol correction to exponential in the settings file. Importantly, this AC algorithm is specifically designed for use in clear to turbid waters and is adaptable to most satellite sensors. However, it is important to note that Acolite requires SWIR bands for effective performance over turbid waters. For this study, we used the 20221114 version of the processor, which is available both as a compiled binary format and as Python source code. Further information can be found on the Institute of Natural Sciences website (https://odnature.naturalsciences.be/remsem/software-and-data/acolite, accessed on 11 July 2024).

(ii) The Polynomial-based algorithm (Polymer) was developed to accommodate waters both with and without sun glint contamination [48]. Polymer operates based on the principle of the spectral matching method, which relies on a polynomial function to characterise the spectral reflectance of both the atmosphere and sun glint. This is achieved by leveraging a water reflectance model applicable to the visible spectrum, further extended to the NIR spectral range (700–900 nm) using a similarity spectrum tailored for turbid waters. Polymer is written in Python, and for this study, we used version v4.16. More information can be found on the HYGEOS website (https://hygeos.com/en/polymer/, accessed on 11 July 2024).

(iii) The Case 2 Regional Coast Colour (C2RCC) is an atmospheric correction algorithm based on Neural Network (NN) principles. Originally developed by [49] under the name "Case 2 Regional processor", the method utilised a substantial collection of radiative transfer simulations inverted by neural networks. Subsequently, the algorithm has been improved, incorporating an additional set of NN computations specifically trained to encompass broader ranges of water scattering and absorption coefficients. This refinement has resulted in the enhanced version available on the European Space Agency (ESA) SentiNel Application Platform (SNAP). In this study, we used version 9.0.

(iv) The Ocean Color—Simultaneous Marine and Aerosol Retrieval Tool (OC-SMART) is a machine learning algorithm that relies on a multilayer neural network (MLNN) classifier driven by extensive radiative transfer simulations. The MLNN used in this processor is a spectral matching algorithm based on the spectral similarity between the Rayleigh corrected TOA and the water leaving radiances. In particular, this approach eliminates the need to retrieve aerosol radiances [50]. It was downloaded from the Light and Life Lab website (http://www.rtatmocn.com/oc-smart/, accessed on 11 July 2024) as a plug-in that was installed in the SNAP platform. OC-SMART is only compatible with SNAP version 7.0, which is the version used to run the plug-in.

Table 2. General information about the selected atmospheric correction processors (ACP).

ACP	Developed by	Implemented in	Where to Get
Acolite	Royal Belgian Institute of Natural Sciences	Phyton	https://odnature.naturalsciences.be/remsem/software-and-data/acolite, accessed on 11 July 2024

C2RCC	European Space Agency	SNAP	https://step.esa.int/main/download/snap-download/, accessed on 11 July 2024
OC-SMART	Stevens Institute of Technology	SNAP v.7	http://www.rtatmocn.com/oc-smart/, accessed on 11 July 2024
Polymer	HYGEOS	Phyton	https://hygeos.com/en/, accessed on 11 July 2024

2.5.2. Assessment of the Spectral Quality of In Situ and Orbital Data

To assess the spectral quality of both the in situ measured and the Sentinel 3 OLCI A and B (S3-OLCI) derived R_{rs} after the applied atmospheric correction, we used the Quality Water Index Polynomial (QWIP) scoring technique [31]. Considering the high sediment content in the Amazon River Continuum waters [23], which leads to a significant magnitude of the R_{rs} spectrum, especially in the red and NIR bands, we chose to use the spectral range from 400 to 800 nm for in situ data and 400 to 779 nm for S3-OLCI bands. QWIP (Equation (8)) is based on a polynomial relationship involving the Apparent Visible Wavelength (AVW) index [51] (Equation (6)) and the Normalised Difference Index (NDI) (Equation (7)). This relationship is established using the red (band 665) and green (band 490) wavelengths. The QWIP score (Equation (9)) is the difference between the AVW and NDI values of a spectrum and the QWIP polynomial. Further information on the method and constant parameters can be found in [31].

$$\mathrm{AVW} = \left(\frac{\sum_{i=1}^{n} R_{rs}(\lambda_i)}{\sum_{i=1}^{n} \frac{R_{rs}(\lambda_i)}{\lambda_i}}\right), \quad (6)$$

$$\mathrm{NDI} = \frac{(R_{rs}(\lambda_2) - R_{rs}(\lambda_1))}{(R_{rs}(\lambda_2) + R_{rs}(\lambda_1))}, \quad (7)$$

$$\mathrm{QWIP} = p_1\mathrm{AVW}^4 + p_2\mathrm{AVW}^3 + p_3\mathrm{AVW}^2 + p_4\mathrm{AVW} + p_5, \quad (8)$$

where $p_1 = -8.399885 \times 10^{-9}$, $p_2 = 1.715532 \times 10^{-5}$, $p_3 = -1.301670 \times 10^{-2}$, $p_4 = 4.357828$, $p_5 = -5.449532 \times 10^{2}$

$$\mathrm{QWIP\ score} = \mathrm{NDI}(490,665) - \mathrm{QWIP}, \quad (9)$$

where an absolute QWIP score threshold of > 0.2 is used to identify spectra of questionable quality [31].

2.5.3. Statistical Indicators for Atmospheric Correction Performance Assessment

In addition to the use of the coefficient of determination R^2 and the slope, other statistical descriptors were used to assess the performance of the atmospheric correction processors considered. These included Root Mean Square Deviation (RMSD), Mean Relative Absolute Difference (MRAD) and mean bias (MB) (Equations (10)–(12)):

$$\mathrm{RMSD} = \left\{\sum_{i=1}^{N} \frac{\left[\log_{10}(\mathrm{Rrs}_i^{AC}) - \log_{10}(\mathrm{Rrs}_i^{obs})\right]^2}{N}\right\}^{1/2}, \quad (10)$$

$$\mathrm{MRAD} = \frac{1}{N} \times \sum_{i=1}^{N} \frac{\left|\mathrm{Rrs}_i^{AC} - \mathrm{Rrs}_i^{obs}\right|}{\mathrm{Rrs}_i^{obs}} \times 100\%, \quad (11)$$

$$\mathrm{MB} = \frac{1}{N} \times \sum_{i=1}^{N} \left|\log10\left(\mathrm{Rrs}_i^{AC}\right) - \log10(\mathrm{Rrs}_i^{insitu})\right|, \quad (12)$$

where Rrs^{obs} is the in situ R_{rs} observations and Rrs^{AC} is the R_{rs} obtained by remote sensing after the atmospheric correction.

Another metric considered here is the number of valid pixels (VP), which takes into account the number of match-ups between in situ measurements and R_{rs} retrieved from the image for the same latitude and longitude.

Radar plots were also used to compare the performance of the AC model tested in this study. This graphical representation allows the visualisation of various statistical parameters condensed into a two-dimensional graph [52]. In this context, an overview of the normalised RMSD, MRAD, MB, slope, R^2 and VP (Equations (13)–(18)) is given. The normalisation process is calculated as follows:

$$\mathrm{RMSD^{norm}\,(j)} = \frac{\mathrm{RMSD(j)}}{\max(\mathrm{RMSD(j)}, \mathrm{j} = 1, \mathrm{k})}, \tag{13}$$

$$\mathrm{MRAD^{norm}\,(j)} = \frac{\mathrm{MRAD(j)}}{\max(\mathrm{MRAD(j)}, \mathrm{j} = 1, \mathrm{k})}, \tag{14}$$

$$\mathrm{MB^{norm}\,(j)} = \frac{\mathrm{MB(j)}}{\max(\mathrm{MB(j)}, \mathrm{j} = 1, \mathrm{k})}, \tag{15}$$

$$\mathrm{Slope^{norm}\,(j)} = \frac{|1 - \mathrm{Slope(j)}|}{\max(|1 - \mathrm{Slope(j)}|, \mathrm{j} = 1, \mathrm{k})}, \tag{16}$$

$$\mathrm{R^{2norm}\,(j)} = \frac{\min\,(\mathrm{R^2(j)}, \mathrm{j} = 1, \mathrm{k})}{\mathrm{R^2}}, \tag{17}$$

$$\mathrm{VP^{norm}(j)} = \frac{\min\,(\mathrm{Vp(j)}, \mathrm{j} = 1, \mathrm{k})}{\mathrm{Vp}}, \tag{18}$$

where *j* represents each individual AC model considered in a defined intercomparison exercise.

In addition to a synthetic visual examination, radar plots were also used to calculate a comprehensive statistical indicator, summarising the overall performance of the AC processor under consideration. In practice, this consists of calculating the area associated with the polygons connecting the normalised indicators from Equations (13)–(18) as follows (Equation (19)):

$$\begin{aligned}\mathrm{Area} = \frac{1}{2} \times \frac{\pi}{6} \times [&\mathrm{RMSD^{norm}\,(j)} \times \mathrm{VP^{norm}\,(j)} + \mathrm{VP^{norm}\,(j)} \times \mathrm{MRAD^{norm}\,(j)} \\ &+ \mathrm{MRAD^{norm}\,(j)} \times \mathrm{MB^{norm}\,(j)} + \mathrm{MB^{norm}\,(j)} \times \mathrm{Slope^{norm}\,(j)} \\ &+ \mathrm{Slope^{norm}\,(j)} \times \mathrm{R^{2norm}\,(j)} + \mathrm{R^{2norm}\,(j)} \times \mathrm{RMSD^{norm}\,(j)}],\end{aligned} \tag{19}$$

An overview of the study process is shown in the following flowchart (Figure 2).

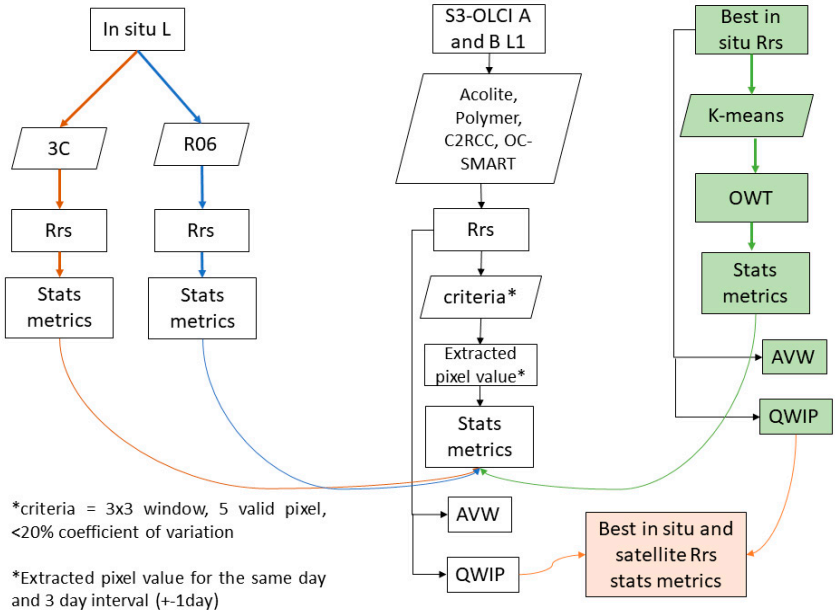

Figure 2. Flowchart of the present study illustrating the overall methodology. The orange, blue and green lines represent the statistical comparisons made between the in situ R_{rs} and the satellite-derived R_{rs} values after atmospheric correction.

3. Results

3.1. Match-Ups

All AC processors tested consistently underestimated the in situ R_{rs}, showing a negative mean bias (Figure 3). However, exceptions were observed for the 665 and 674 nm bands of OC-SMART (Figure 4). The Acolite processor showed higher R^2 values for most bands and a lower RMSD compared to other AC processors. The RMSD showed a similar pattern for all processors, with high values at lower wavelengths, decreasing until reaching the NIR, at which point the values increased again. Except for Acolite, the RMSD at 620 nm showed a peak with high values for all AC processors. Compared to the other AC processors, Acolite showed mean bias values closer to zero, indicating that it was the processor that least underestimated R_{rs} retrievals (Figure 4).

Looking more closely at the match-ups on a band-to-band basis, it becomes apparent that the accuracy of the retrievals varied depending on the wavelength. This band-to-band variation has also been observed by [53] for different ACs, including Polymer and C2RCC. For the bands from 400 to 510 nm, the scattering of the retrievals was consistently high across all AC processors. However, it is noteworthy that within this range, Acolite showed superior performance compared to the other AC processors (Figure 3).

There is a marked increase in R^2 as the wavelengths move from the blue to the red part of the spectrum, peaking at 665 nm, 674 nm, and 681 nm. There is then a decrease as the bands enter the NIR region (Figure 4). MRAD shows the same trend for all AC processors, with higher values at the extremes of the spectrum and lower values in the green region, except for OC-SMART, which shows a peak between the bands of 620–754 nm. This MRAD peak corresponds to an increase in the average bias of the OC-SMART R_{rs} (Figure 4).

The 3 h time difference between in situ and satellite measurements appears to be more significant for C2RCC than for the other AC processors (Figure 3). Although C2RCC had significantly more valid pixels, it also had the worst retrieval performance, with low coefficients of determination (R^2) and high RMSD values for all bands (Figure 4).

With the exception of Acolite, which showed a distinct pattern, the slope of the regression line showed a consistent trend of increasing with the wavelength. The peak

occurred between the 665 and 709 nm bands, after which the slope decreased abruptly (Figure 4).

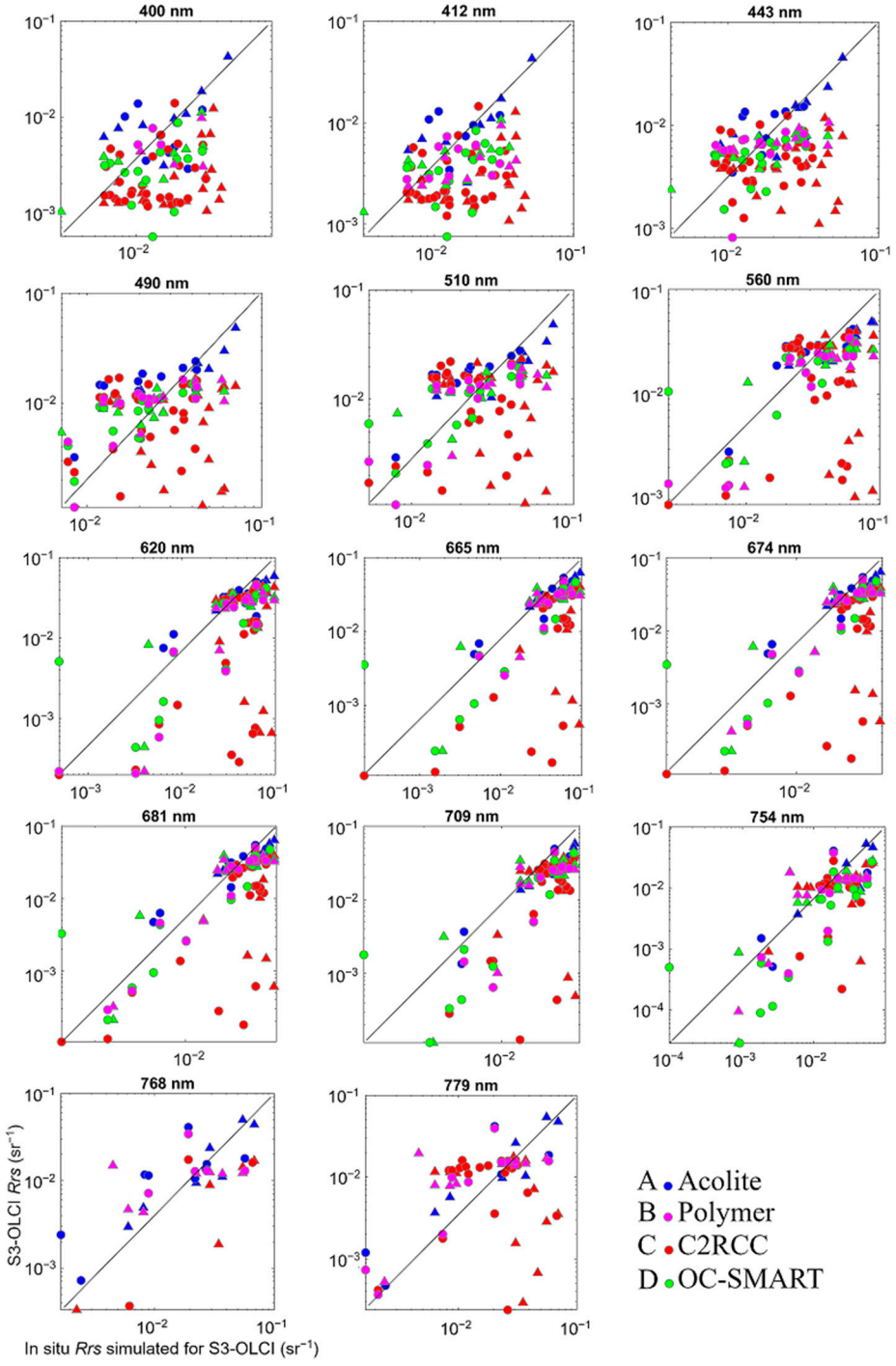

Figure 3. Match-ups of simulated in situ R_{rs} for S3-OLCI bands and R_{rs} derived from different atmospheric correction processors for the same day: (**A**) Acolite; (**B**) Polymer; (**C**) C2RCC; (**D**) OC-SMART. The data were measured at the Amazon River Continuum, and the in situ R_{rs} were derived following the methodology proposed by [37] with the elimination of sun and sky glint as recommended by [38]. Scatter plots are presented in a log–log scale. Circles represent match-ups within a 3 h satellite pass window, while triangles represent match-ups outside the 3 h satellite pass window.

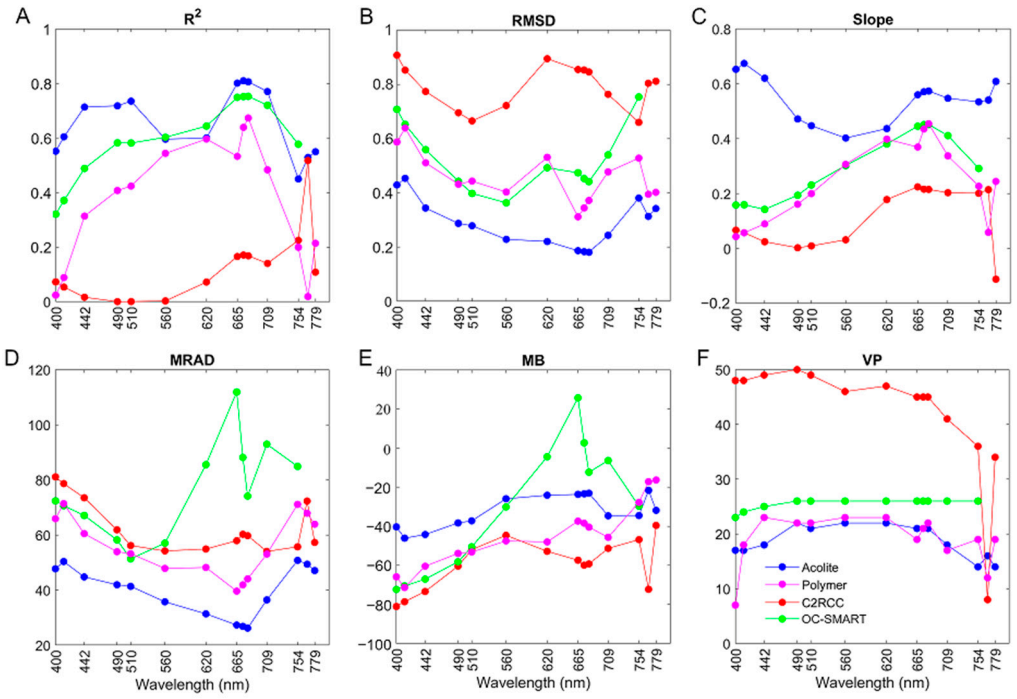

Figure 4. Spectral variation in the statistical parameters between 400 and 779 nm: (**A**) Coefficient of determination (R^2), (**B**) Root Mean Square Deviation (RMSD), (**C**) slope, (**D**) Mean Relative Absolute Difference (MRAD), (**E**) Mean Bias (MB) and (**F**) Valid Pixel (VP).

We assessed the feasibility of including measurements from one day before or after the in situ measurement and investigated whether the 3C model agrees with our in situ data. To provide an overview, we compare all the bands together (Figure 5). A smaller area on the radar plot indicates better results.

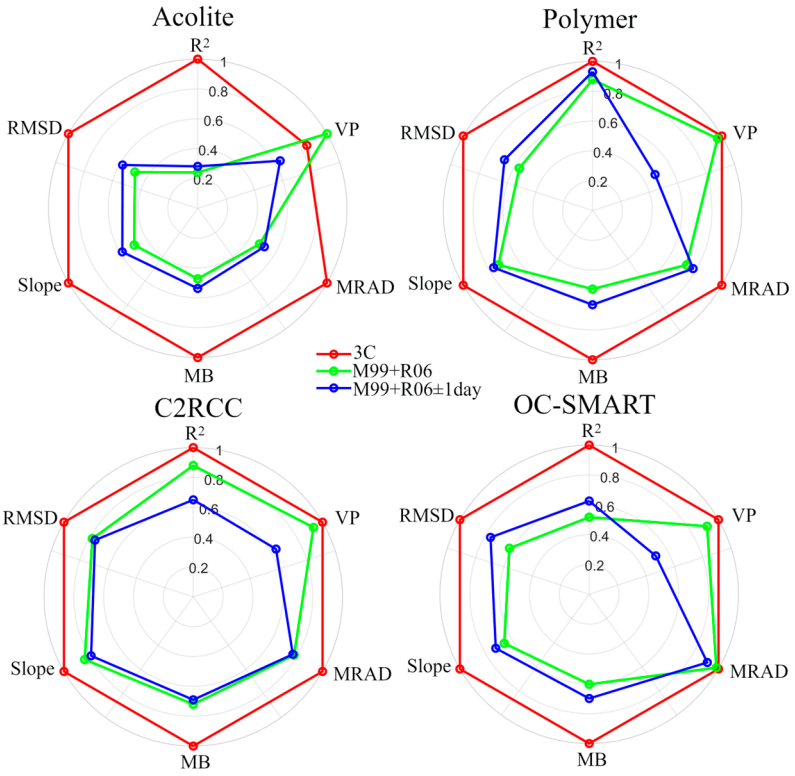

Figure 5. Radar plot illustrating the statistical metrics used to evaluate the accuracy of the remote sensing reflectance for each atmospheric correction processor, using different approaches to estimate in situ R_{rs}. The green line represents the in situ R_{rs} processed according to [37] with sun and sky glint corrected according to the method proposed in [38] (M99 + R06). The blue line shows the same approach, not only considering the day of the in situ measurement but also one day before or after to increase the number of match-ups. The red line corresponds to the in situ R_{rs} processed with the 3C model.

Clearly, the 3C model showed poor performance with our data (area size: Acolite = 1.53; Polymer = 1.57; C2RCC = 1.57; OC-SMART = 1.57, Table A1), resulting in suboptimal agreement with the R_{rs} obtained from the post-atmospheric correction image. We also continued the evaluation using only the in situ R_{rs} processed by the M99 + R06 method. While restricting the data to the same day as the in situ measurement gave slightly better results for most of the AC processors (area size: Acolite = 0.37; Polymer = 0.77; C2RCC = 1.03; OC-SMART = 0.81, Table A2), including data from one day before or after did not significantly affect the results (area size: Acolite = 0.41; Polymer = 0.85; C2RCC = 0.83; OC-SMART = 0.85, Table A3). Therefore, for this study area, the number of match-ups could be increased if necessary. In our case, including data from one day before or after increased the number of match-ups by 57% for Acolite, 100% for Polymer, 46% for C2RCC and 77% for OC-SMART.

3.2. Optical Water Types at the Amazon River Continuum

To assess the optical variability within the dataset, we employed k-means classification, which resulted in the identification of five distinct OWTs. In particular, OWT K5 (Figure 6A) exhibited optical properties similar to those of oceanic waters, characterised by increased reflectance at shorter wavelengths and increased absorption at longer wavelengths [40]. Most of cluster K5 (in blue, Figure 6B) lies below the Amazon River estuary and is not under the influence of the Amazon River, whose plume is known to extend north-westwards towards French Guiana [36,54]. Consequently, from this point on, all spectra from this class were removed from our analysis, ensuring that only waters with the Amazon River Continuum signal were assessed.

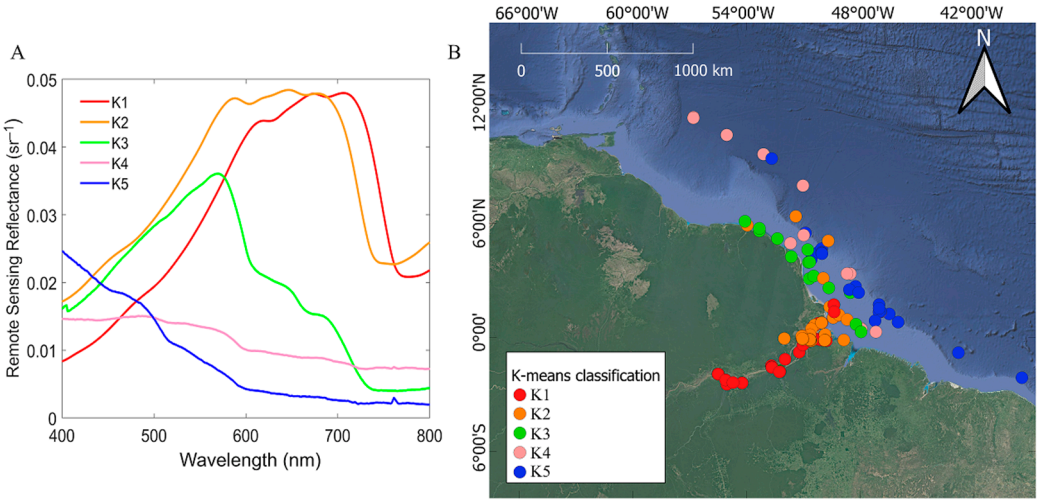

Figure 6. (**A**) Optical Water Types (OWT) identified in the Amazon River Continuum and (**B**) their location for the different campaigns carried out (see Figure 1 and Table 1 for more information on the field campaigns).

OWTs K1 and K2 characterise sediment-laden waters, mainly along the Lower Amazon [23] (Valerio et al., 2021). Conversely, OWTs K3 and K4 are predominantly found in

coastal waters, with their spectral signatures indicating the prevalent presence of chla (K3) and a covariance of other bio-optical parameters (K4) [23,55].

3.3. Assessment of the Spectral Quality

3.3.1. In Situ R_{rs}

To ensure the spectral quality of the final dataset (in situ R_{rs} simulated on S3-OLCI bands after the removal of the K5 spectrum and extracted OLCI for match-ups, except for those from K5 OWT), we applied the AVW and QWIP score method on the remaining spectra. Considering the entire dataset (excluding the K5 OWT determined by k-means), out of a total of 203 in situ R_{rs} spectra, only 25% are considered valid when applying the recommended range of −0.2 to 0.2 [31], indicating that these spectra "pass" the quality assessment. On closer inspection, there is considerable variability between the different OWTs. The first two OWTs (K1 and K2), located mainly in the Amazon River and adjacent coastal waters with higher sediment content, have a higher failure rate, with only 14% and 4% considered to be of adequate quality. In contrast, OWTs K3 and K4, located in the coastal waters of Brazil and the outer reaches of the Amazon River Plume, have higher validity rates of 94% and 81%, respectively (Table 3). All spectra from OWT K1 and K2 that did not pass the QWIP score had values < −0.2, a pattern also observed and discussed by [31] and attributed to optically shallow waters. Conversely, our study area does not exhibit characteristics of optically shallow waters; rather, the problem arises when the AVW > 580 nm (Figure 7), where absolutely all of our K1 fits with the AVW mean of 614 nm and 90% of our OWT K2 fits with an AVW mean of 592 nm. For this reason, we have relaxed the QWIP score threshold to the range between −0.3 and 0.3 for these two OWTs (K1 and K2).

Table 3. Percentage of valid in situ R_{rs} spectra after the QWIP score evaluation. The right column shows the percentage of valid in situ R_{rs} spectra considering a range from −0.2 to 0.2. The left column shows the percentage of valid in situ R_{rs} spectra considering a range from −0.3 to 0.3.

OWT (N)	−0.2 to 0.2	−0.3 to 0.3
All (203)	25%	80%
K1 (97)	14%	89%
K2 (67)	4%	60%
K3 (16)	94%	94%
K4 (21)	81%	95%

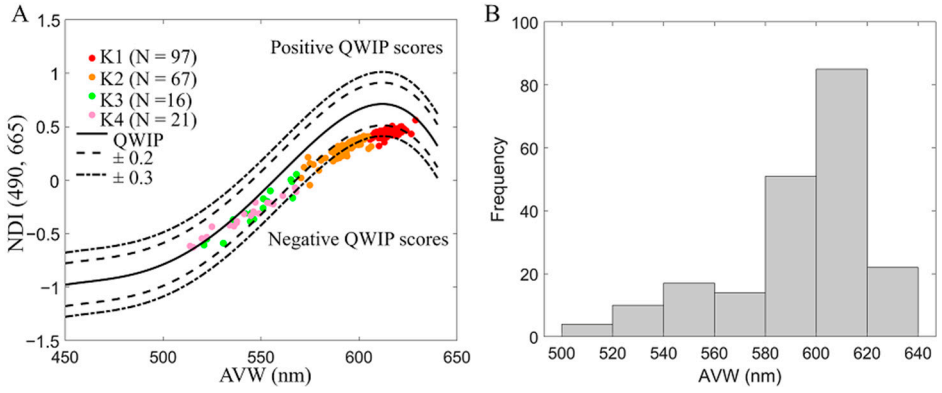

Figure 7. (**A**) The QWIP relationship between Apparent Visible Wavelength (AVW) and the Normalised Difference Index (NDI) at blue-green and red bands, as described in [31], with the Amazon River Continuum (ARC) in situ R_{rs} dataset showing the different levels of QWIP values (±0.2 dashed grey line and ±0.3 dash-dotted grey line). Each optical water type found at the ARC is represented by a different colour. (**B**) Histogram of the AVW for our in situ ARC dataset.

3.3.2. S3-OLCI R_{rs}

The AVW and QWIP scoring methods were also applied to S3-OLCI images resulting from the four atmospheric corrections. As an example, we choose the 8 November 2019 image at the Amazon River mouth to represent the application of the AVW in the images (Figure 8).

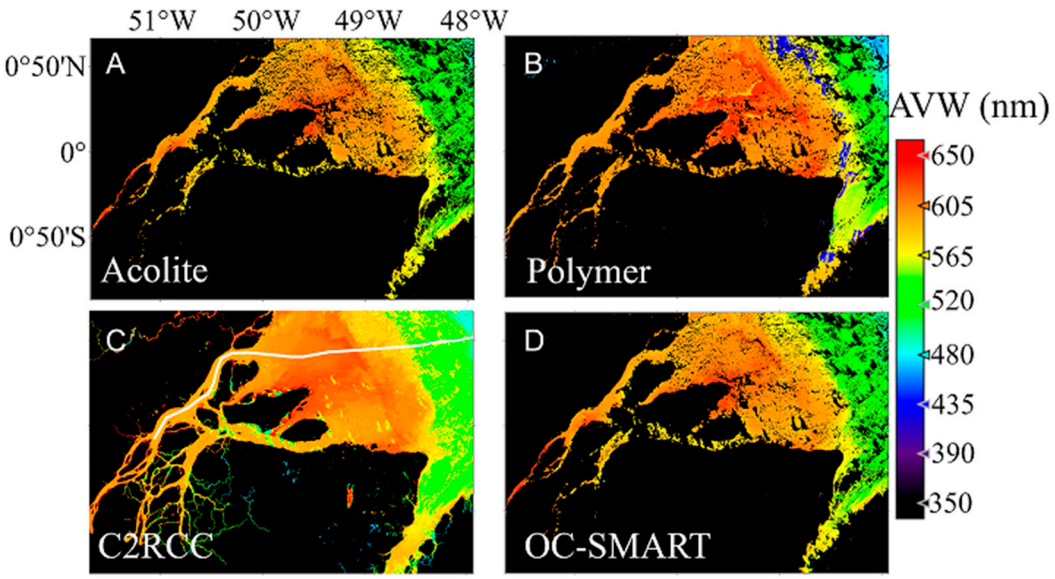

Figure 8. Mapped S3-OLCI image as an example (8 November 2019), where Apparent Visible Wavelength has been applied after using different atmospheric corrections: (**A**) Acolite; (**B**) Polymer; (**C**) C2RCC and (**D**) OC-SMART. The white line in the C2RCC image represents the transect used to extract pixels for evaluation. The same transect was applied to all four images processed with different atmospheric corrections.

The AVW results are strongly influenced by the AC method used (Figures 8 and 9, Table A4). Despite having similar values, the same pixel lacks consistency when processed with different atmospheric corrections. Images processed with the Polymer processor show higher AVW values in an overall basic statistic, while OC-SMART shows lower AVW values (Table A4).

We traced a transect extending from the river mouth to the inner plume (white line in Figure 8 on the C2RCC image) to examine the pixel variations along this path (Figure 9). It is clear that Acolite and C2RCC have higher variability, which increases towards the oceanic region. Conversely, Polymer and OC-SMART show lower variability, although there is noticeable noise in the Polymer image, indicated by the dark blue patches (Figure 8). OC-SMART stands out as having lower AVW values compared to the other AC-processed images. This consistently lower AVW trend for OC-SMART is also evident (Table A4).

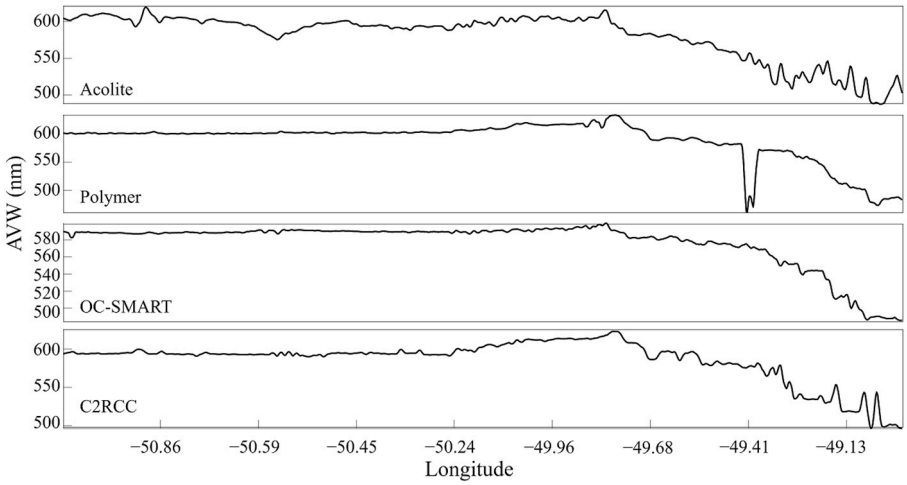

Figure 9. Apparent Visible Wavelength (AVW) values for the same pixel according to different atmospheric correction approaches, with longitudinal variability.

The QWIP score was calculated for each image using different AC approaches (Figure 10). As observed, more pixels from the OC-SMART were considered to be valid (in the range of −0.2 to 0.2) compared to other AC approaches. It is also noticeable that pixels with negative values are concentrated in the Amazon River and adjacent waters, while positive values are concentrated closer to oceanic waters.

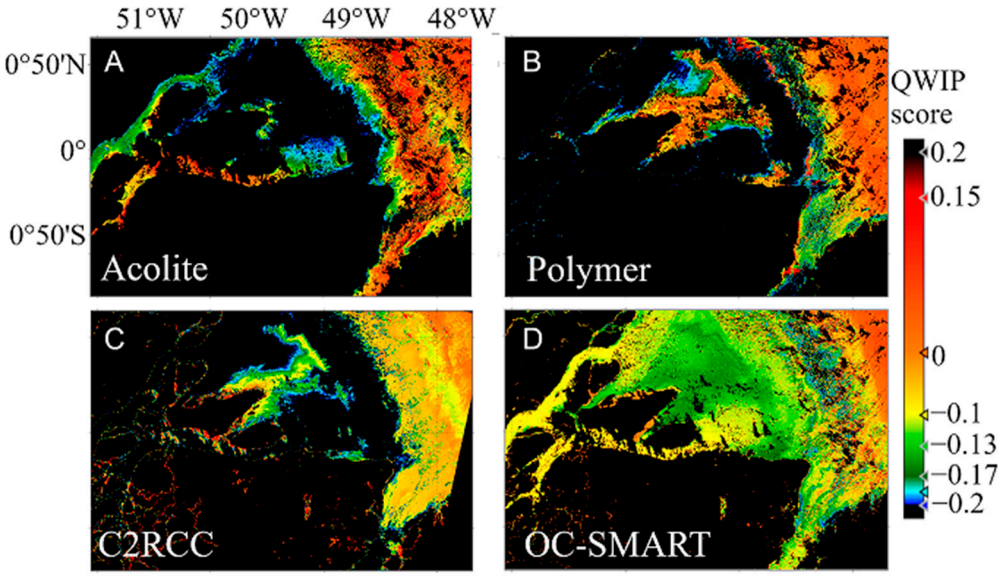

Figure 10. Mapped S3-OLCI image as an example (8 November 2019), where Quality Water Index Polynomial score was calculated after applying different atmospheric corrections: (**A**) Acolite; (**B**) Polymer; (**C**) C2RCC and (**D**) OC-SMART. Black pixels are those outside the range of −0.2 to 0.2, as recommended by [31]. Pixels outside this range are considered as not passing the spectral quality.

After calculating the QWIP score for each pixel in the images processed using the four AC approaches, we again performed a match-up comparison with the good quality in situ data to assess whether there was any improvement in the results. Using the QWIP score interval (−0.2 to 0.2) in the images to retain only those pixels that passed the spectra quality threshold, we observed utilisation rates of 65%, 71%, 94% and 43% for Acolite, C2RCC, OC-SMART and Polymer, respectively (Table A5).

This means that more data were used from C2RCC and OC-SMART compared to Acolite and Polymer, the latter having fewer pixels passing the QWIP score interval. The results show a slight improvement with an overall reduction in the scattering of the retrievals (Figure 11) when compared to the results in Figures 3 and 4.

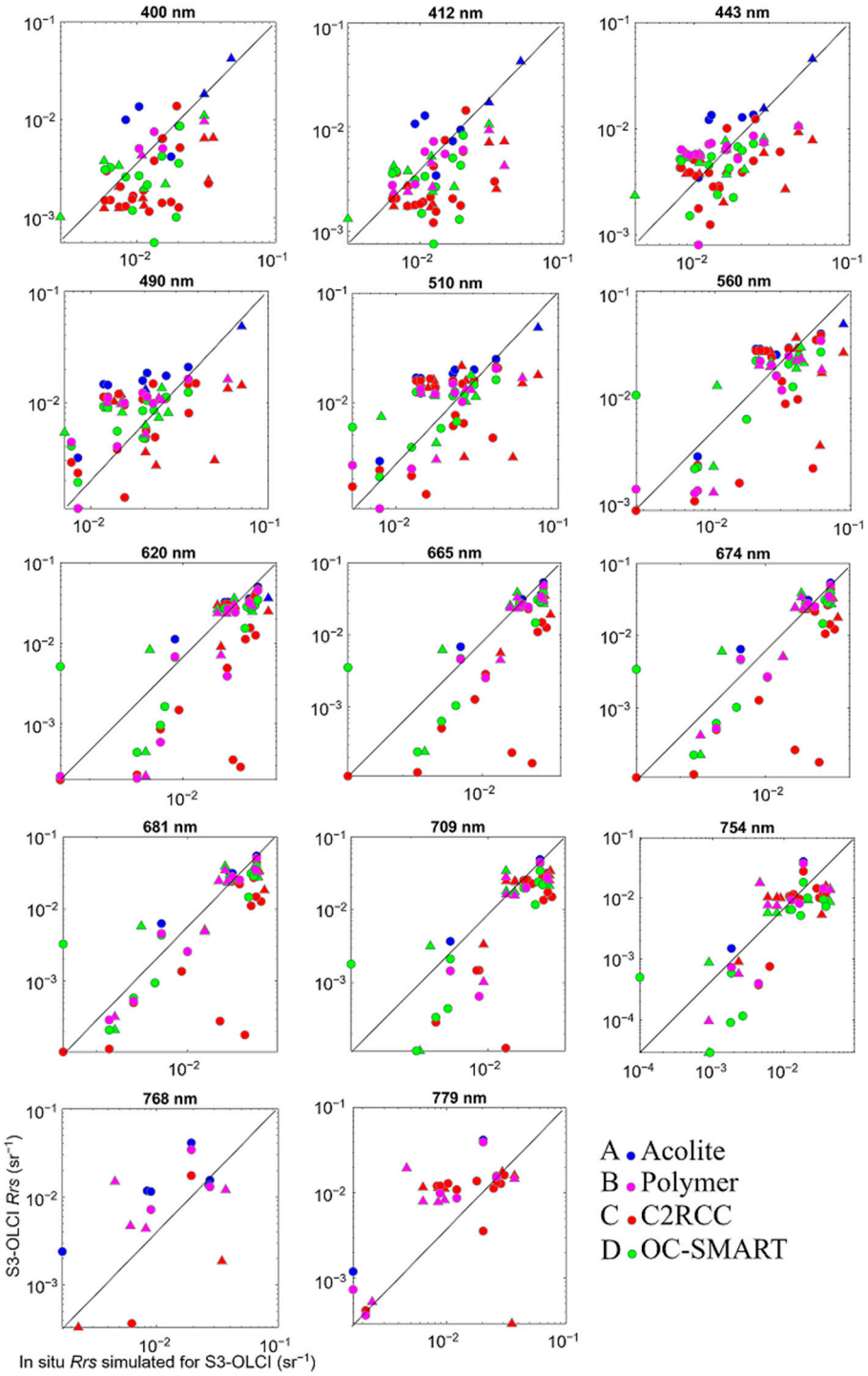

Figure 11. Match-ups of simulated in situ R_{rs} for S3-OLCI bands and R_{rs} derived from different atmospheric correction processors for the same day: (**A**) Acolite; (**B**) Polymer; (**C**) C2RCC; (**D**) OC-SMART. The in situ and satellite data used for the match-up passed the QWIP score with an interval of ±0.3. The data were measured at the Amazon River Continuum, and the in situ R_{rs} were derived following the methodology proposed by [37] and the elimination of sun and sky glint as recommended by [38]. Scatter plots are presented on a log–log scale. Circles represent match-ups within

a 3 h satellite pass window, while triangles represent match-ups outside the 3 h satellite pass window.

After applying the QWIP score, there was an increase in the coefficient of determination, with values close to one in the blue region of the wavelengths for the Acolite processor. The MRAD did not show any significant changes before and after the QWIP score, while the MB showed a slight improvement (Figure 12). The Acolite had fewer valid pixels compared to the other ACs.

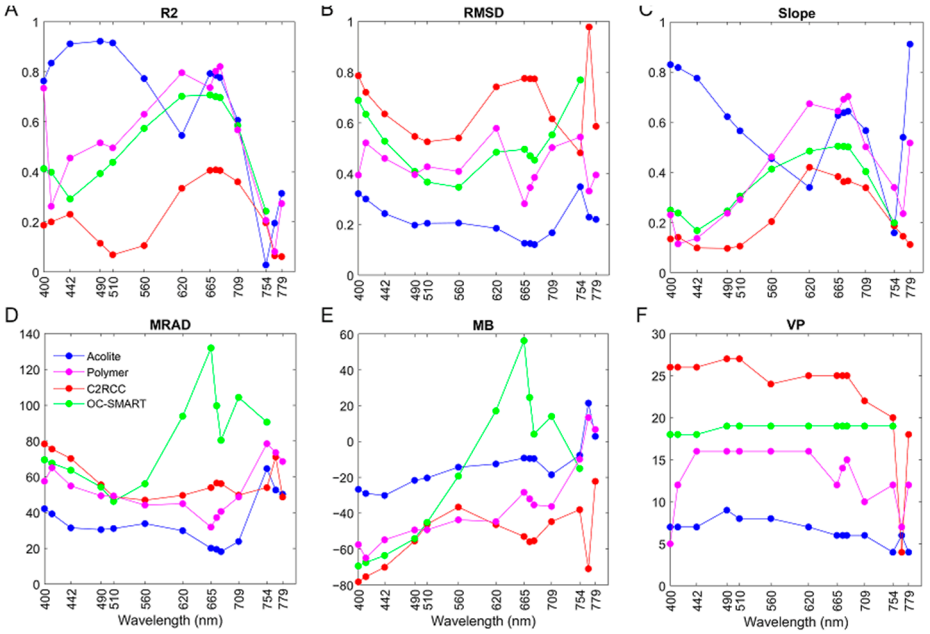

Figure 12. Spectral variation in the statistical parameters between 400 and 779 nm for the in situ and satellite data that passed the QWIP score with an interval of ±0.3: (**A**) Coefficient of determination (R^2), (**B**) Root Mean Square Deviation (RMSD), (**C**) Slope, (**D**) Mean Relative Absolute Difference (MRAD), (**E**) Mean Bias (MB) and (**F**) Valid Pixel (VP).

4. Discussion

To our knowledge, no study has been conducted using S3-OLCI in Amazon waters to investigate differences in atmospheric correction and remote sensing reflectance. Our study showed a high scatter in the retrievals in the lower wavelength bands (<510 nm) (Figure 3), and this is especially true for the R_{rs} corrected with C2RCC. This scattering persists even in higher wavelength bands for this AC processor, unlike other processors that remain closer to the 1:1 line. The low performance of the C2RCC is to be expected, as the training data used to train its neural network consisted mainly of simulations of the Hydrolight model and samples from European waters [56], where water constituents and bio-optical properties differ considerably from those found in the extremely turbid waters of the Amazon River Continuum.

A study conducted by [30] examined two coastal waters: (i) those of French Guiana, which are seasonally influenced by the turbid waters of the Amazon River plume, and (ii) the Eastern English Channel, which is characterised by moderately turbid waters.

They also used S3-OLCI images but used different atmospheric correction processors to those used in our study. Their results showed similarly high scatter in the R_{rs} retrievals in the lower wavelength bands (400–443 nm). According to the statistical metrics presented in Figure 4, the spectral variation shows significant differences depending on the AC applied. Nevertheless, our results consistently show an underestimation of the R_{rs} for all AC processors tested. This consistent underestimation was also observed in highly turbid waters when using different AC processors for S3-OLCI [57].

When comparing the four AC methods tested, Acolite showed the best performance with a smaller area size, followed by Polymer (area size: Acolite = 0.37; Polymer = 0.77; C2RCC = 1.03; OC-SMART = 0.81) (Figure 5, Table A2). However, it is important to note that Acolite had fewer valid pixels compared to the other ACs, which could pose a challenge for match-up exercises and validation. Furthermore, the Amazon region is known for its high cloud cover, which also complicates data retrieval using water colour remote sensing. Previous studies have shown that Polymer also performed better, producing a higher number of match-ups because it worked well even under conditions of high sun glint and high aerosol loads. However, it also underestimated R_{rs} for turbid waters [53].

The Amazon River has a unique water colour due to its high turbidity. In this study, we aimed to evaluate whether the 3C model, which is recommended to improve the estimation of R_{rs} using above-water radiometric measurements can provide accurate R_{rs} estimates in such environments. Typically, above-water measurements, such as those conducted in this study, are susceptible to significant contributions from sun glint and reflected sky radiance [58]. While previous studies have reported satisfactory results with the 3C model for optically complex water systems [32], our results were not consistent with those in our study area. Contrary to expectations, the 3C model underestimated values obtained by different AC processors (Table A1) and showed poor statistical metrics (Figure 5). The discrepancies between R_{rs} calculated from [37] and the 3C model may be due to water or atmospheric properties that the 3C model could not accurately reconstruct. It is expected that the 3C model would provide lower R_{rs} values [58]. Therefore, the calculation of R_{rs} according to [37], followed by the sun glint correction proposed by [38], which is recommended for turbid waters, proved to be the most appropriate method for our study area. Including data from one day before or after did not significantly affect the results, as shown in Figure 5. This can be attributed to the fact that the optical variability of the Amazon River is determined by the hydrological regime. Therefore, it could be expected that the water colour would not vary significantly within one or two days during the same hydrological season.

The four OWTs identified in this study have also been discussed by other authors in the context of Amazonian waters or highly turbid waters. In their study [23], they showed that the difference between OWT K1 and K2 lies in the amount of sediment content resulting from the seasonal discharge of the Amazon River. OWT K1 typically occurs during the rising water season, which is characterised by a significant sediment input, resulting in a three times higher absorption coefficient of particulate matter (a_{P}) compared to the absorption coefficient of coloured dissolved organic matter (a_{CDOM}) [23]. During the rest of the year, the ratio of a_{P} to a_{CDOM} in the Amazon River is close to 1:1, defining OWT K2. The OWTs K3 and K4 have also been identified in other studies assessing global inland and coastal OWTs [40,55]. They represent coastal waters where the optical signals are predominantly influenced by phytoplankton and a mixture of covarying bio-optical parameters, respectively.

It is not the intention of this study to perform a validation match-up comparison of OWT's R_{rs} for the AC processors evaluated. In fact, we would need more samples to perform such an analysis. However, based on the available data and using the same statistical metrics defined in our methods, preliminary results indicate that there is an interval in the spectrum between 490 and 709 nm where all ACs showed better performance (Figure 13). Conversely, the blue region between 400 and 443 nm showed lower performance.

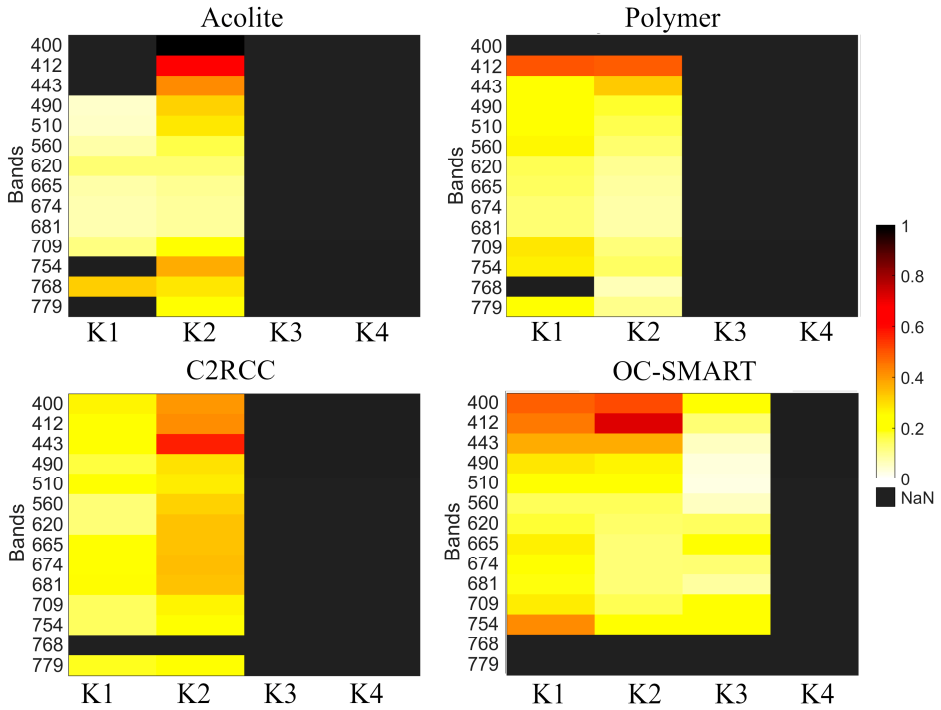

Figure 13. Performance evaluation according to the statistical metrics (R^2, RMSD, MRAD, MB, VP). Light colours (white or yellow, closer to 0) are likely to have accurate R_{rs} for a given optical water type (OWT: K1, K2, K3 and K4) and S3-OLCI band.

Preliminary results also suggest that Acolite performed better for OWT K1 but also showed good performance for K2, similar to Polymer (Figure 13). On the other hand, OC-SMART showed better performance for K3, which is characterised by coastal waters with higher chla. Unfortunately, there are insufficient data to perform this analysis for all ACs for OWT K4, and the same limitation applies to OWT K3 for Acolite, C2RCC, and Polymer. Although [27] used different orbital sensors (Landsat 8 and S2-MSI), their results appear to be consistent with our preliminary results. They found that Acolite performed better in highly turbid inland waters, while OC-SMART showed good accuracy in clearer waters. As mentioned, further studies are still needed, but preliminary results show that different AC methods may perform better in retrieving R_{rs} depending on the OWT. This knowledge may be useful if the OWT system is matched to the performance of the atmospheric correction [59].

Using the QWIP score as a quality control method for in situ and orbital R_{rs} data has been recommended by recent studies [32,59] and may even help to determine the best AC method to use in a given study area [32]. While [31] recommend using a range of ±0.2 to ensure high-quality data, other authors suggest that this range can be relaxed to ±0.3 when working with multispectral data such as S3-OLCI [59]. If we extend this range to ±0.3 for both in situ and orbital data, we observe a data utilisation rate of over 80% for the OWTs defined in this study using in situ data, except for K2, and a pixel utilisation rate of over 95% in the images for all atmospheric correction methods. Polymer, in particular, benefits significantly from this relaxation, more than doubling the number of usable pixels. The prospect of obtaining more usable pixels in Polymer images is promising, given that it has been specifically designed to minimise the effect of sun glint [48]. Given the Amazon region's notorious propensity for high glint effects in satellite imagery [60], the use of Polymer could prove highly beneficial.

Relaxing the QWIP score range had little effect on the OC-SMART images, which increased from 94% to 97% (Table A5). Finally, after applying the QWIP score to in situ and orbital R_{rs} corrected by different AC methods, Acolite still has the smallest area,

followed by Polymer (area size: Acolite = 0.36; Polymer = 0.69; C2RCC = 1.17; OC-SMART = 0.95, Table A6).

5. Conclusions

This study on the evaluation of atmospheric corrections for S3-OLCI imagery in the Amazon River Continuum revealed several important findings. First, the tested AC methods consistently underestimated R_{rs} compared to in situ measurements. In particular, the 3C model showed poorer performance than the traditional M99 + R06 approach in our study area, which is characterised by very turbid waters. Of the AC processors tested, Acolite had the best overall performance, followed by Polymer and OC-SMART, while C2RCC had the lowest performance. Examination of the R_{rs} match-ups band by band revealed increasing coefficients of determination with wavelengths up to bands 665 nm, 674 nm, and 681 nm ($R^2 \approx 0.8$ for Acolite), followed by a decrease in the near-infrared spectral range. It is also worth noting that there is a peak in the RMSD in the 620 nm band for Polymer, OC-SMART and C2RCC. Using a match-up interval of 3 days (±1 day) slightly increased the error but did not significantly affect the results, making it a viable option to increase the number of observations for match-up analysis if required. This is because the optical variability of the Amazon River is determined by the hydrological regime. It was therefore expected that the water colour would not vary greatly within a day or two during the same hydrological season.

In addition, four OWTs under the influence of the Amazon River Continuum were identified. Two of these OWTs are typically associated with the Amazon River and show seasonal variations in response to changes in Amazon River discharge. The other two OWTs are typically associated with the Amazon River Plume. One of these OWTs is characterised by the dominance of chla, while the other exhibits a mixture of covarying bio-optical parameters.

Furthermore, the QWIP score range of −0.2 to 0.2 was found to be inadequate for very turbid waters, such as those represented by OWTs K1 and K2, where AVW > 580 nm. The results also highlighted the dependence of AVW results on the AC method used. Overall, the OC-SMART R_{rs} products showed superior spectral quality compared to other AC processors.

Further studies are warranted to assess the impact of different optical water types on the retrieval of R_{rs} with respect to atmospheric correction methods. It is important to note that OWTs are not only determined by the bio-optical properties found in a geographic location; seasonal variations also play an important role. Therefore, if an AC processor performs well in a particular region during a particular season, this does not guarantee optimal performance during another season of the year.

Finally, it is worth noting that, as emphasised by previous studies, there is no consensus on which AC method is superior, as this depends on specific scientific objectives and applications [27,30]. Furthermore, it is important to keep in mind that atmospheric correction processors are constantly evolving, and the methodology used in this study only captures a momentary perspective of the current state.

Author Contributions: Conceptualisation, A.M.V., M.K. and V.V.; Data curation, A.M.V.; Formal analysis, A.M.V., M.K. and V.V.; Funding acquisition, M.K. and J.R.; Investigation, A.M.V., M.K. and V.V.; Methodology, A.M.V., M.K. and V.V.; Project administration, V.B. and J.R.; Resources, M.K. and J.R.; Software, A.M.V.; Supervision, M.K., V.V., V.B. and J.R.; Validation, A.M.V.; Writing—original draft, A.M.V.; Writing—review and editing, A.M.V., M.K., V.V., V.B. and J.R. All authors have read and agreed to the published version of the manuscript.

Funding: This research was funded by São Paulo Research Foundation (FAPESP 2018/18491-4, 2020/08148-0 and 2021/04128-8), and by U.S. National Science Foundation DEB-1754317. This work was partially financed by the Coordenação de Aperfeiçoamento de Pessoal de Nível Superior—Brazil (CAPES)—Finance Code 001, Agência Espacial Brasileira (AEB) and Instituto Nacional de Pesquisas Espaciais (INPE).

Data Availability Statement: The Sentinel-3 OLCI images used in this study can be accessed at CREODIAS and Copernicus Data Hub. In situ radiometric data can be made available to interested users, subject to prior consultation with the authors of this study.

Acknowledgments: The authors thank Andrea de Lima Oliveira, Gabriel Moiano Cesar, João Felipe Santos e Vitor Galazzo for in situ sampling during field campaigns. We also would like to thank the collaborators from the Monitoring Oceans from the Space Laboratory from the National Institute for Space Research (MOceanS-INPE) and the TROCAS team. We appreciate the value of the Copernicus program for providing full and free-of-charge access to Sentinel-3 OLCI imagery. We also recognize the value of the developers of free-of-charge SNAP software (version 7.0 and version 9.0 used in this study) for providing image process tools.

Conflicts of Interest: The authors declare no conflicts of interest.

Appendix A

Table A1. Statistical metrics (R^2, slope, Root Mean Square Deviation—RMSD, Mean Relative Absolute Difference—MRAD, mean bias—MB, and valid pixel—VP), using the 3C model to calculate R_{rs} and applying different atmospheric correction procedures. These statistics use satellite data from the same day as the in situ measurement.

	Acolite	Polymer	C2RCC	OC-SMART
R^2	0.18	0.48	0.20	0.36
RMSD	0.60	0.81	1.02	0.86
SLOPE	0.157	0.168	0.102	0.146
MB	0.50	0.72	0.85	0.74
MRAD	81	75	80	78
VP	313	258	552	279
AREA	1.53	1.57	1.57	1.57

Table A2. Statistical metrics (R^2, slope, Root Mean Square Deviation—RMSD, Mean Relative Absolute Difference—MRAD, mean bias—MB, and valid pixel—VP), using [37,38] to calculate R_{rs} and correct for sun glint and sky radiance. These statistics use satellite data from the same day as the in situ measurement.

	Acolite	Polymer	C2RCC	OC-SMART
R^2	0.74	0.54	0.23	0.70
RMSD	0.29	0.46	0.80	0.53
SLOPE	0.59	0.39	0.25	0.44
MB	0.24	0.38	0.61	0.45
MRAD	39	55	62	76
VP	264	267	591	306
AREA	0.37	0.77	1.03	0.81

Table A3. Statistical metrics (R^2, slope, Root Mean Square Deviation—RMSD, Mean Relative Absolute Difference—MRAD, mean bias—MB, and valid pixel—VP), using [37,38] to calculate R_{rs} and correct for sun glint and sky radiance. These statistics include data from satellite images taken one day before or after the in situ measurement.

	Acolite	Polymer	C2RCC	OC-SMART
R^2	0.63	0.51	0.31	0.58
RMSD	0.35	0.55	0.77	0.66
SLOPE	0.51	0.36	0.29	0.38
MB	0.27	0.45	0.59	0.52
MRAD	42	58	62	71
VP	414	534	863	542
AREA	0.41	0.85	0.83	0.85

Table A4. Basic statistics of the Apparent Visible Wavelength (AVW) in the Amazon River Continuum according to the different atmospheric correction processors used in this study (Acolite, Polymer, C2RCC and OC-SMART).

	Acolite	Polymer	C2RCC	OC-SMART
Min	475	440	455	453
Max	650	700	681	631
Mean	577.8	586.2	582.8	572.1
Median	588.9	600.5	593.5	587.5

Table A5. Percentage of valid pixel R_{rs} spectra after the Quality Water Index Polynomial (QWIP) score evaluation. The right column shows the percentage of valid pixel R_{rs} spectra considering a range from −0.2 to 0.2. The left column shows the percentage of valid pixel R_{rs} spectra considering a range from −0.3 to 0.3.

AC	−0.2 to 0.2	−0.3 to 0.3
Acolite	65%	100%
Polymer	43%	96%
C2RCC	71%	100%
OC-SMART	94%	97%

Table A6. Statistical metrics (R^2, slope, Root Mean Square Deviation—RMSD, Mean Relative Absolute Difference—MRAD, mean bias—MB, and valid pixel—VP), using [37,38] to calculate R_{rs} and correct for sun glint and sky radiance. These statistics use satellite data from the same day as the in situ measurement. Quality Water Index Polynomial score was used to improve the relationship between in situ and satellite data.

	Acolite	Polymer	C2RCC	OC-SMART
R^2	0.70	0.57	0.39	0.66
RMSD	0.22	0.45	0.67	0.53
SLOPE	0.60	0.55	0.36	0.51
MB	0.18	0.35	0.52	0.43
MRAD	34	52	58	80
VP	91	182	328	225
AREA	0.36	0.69	1.17	0.95

References

1. Ward, N.D.; Bianchi, T.S.; Medeiros, P.M.; Seidel, M.; Richey, J.E.; Keil, R.G.; Sawakuchi, H.O. Where Carbon Goes When Water Flows: Carbon Cycling across the Aquatic Continuum. *Front. Mar. Sci.* **2017**, *4*, 7. https://doi.org/10.3389/fmars.2017.00007.
2. Xenopoulos, M.A.; Downing, J.A.; Kumar, M.D.; Menden-Deuer, S.; Voss, M. Headwaters to Oceans: Ecological and Biogeochemical Contrasts across the Aquatic Continuum. *Limnol. Oceanogr.* **2017**, *62*, S3–S14. https://doi.org/10.1002/lno.10721.
3. Billen, G.; Lancelot, C.; Meybeck, M. N, P, and Si Retention along the Aquatic Continuum from Land to Ocean. In *Ocean Margin Processes in Global Change*; John Wiley & Sons: Hoboken, NJ, USA, 1991; pp. 19–44, ISBN 0471926736.
4. Medeiros, P.M.; Seidel, M.; Niggemann, J.; Spencer, R.G.M.; Hernes, P.J.; Yager, P.L.; Miller, W.L.; Dittmar, T.; Hansell, D.A. A Novel Molecular Approach for Tracing Terrigenous Dissolved Organic Matter into the Deep Ocean. *Glob. Biogeochem. Cycles* **2016**, *30*, 689–699. https://doi.org/10.1002/2015GB005320.
5. Medeiros, P.M.; Seidel, M.; Ward, N.D.; Carpenter, E.J.; Gomes, H.R.; Niggemann, J.; Krusche, A.V.; Richey, J.E.; Yager, P.L.; Dittmar, T. Fate of the Amazon River Dissolved Organic Matter in the Tropical Atlantic Ocean. *Glob. Biogeochem. Cycles* **2015**, *29*, 677–690. https://doi.org/10.1002/2015GB005115.
6. Weber, S.C.; Carpenter, E.J.; Coles, V.J.; Yager, P.L.; Goes, J.; Montoya, J.P. Amazon River Influence on Nitrogen Fixation and Export Production in the Western Tropical North Atlantic. *Limnol. Oceanogr.* **2017**, *62*, 618–631. https://doi.org/10.1002/lno.10448.
7. Goes, J.I.; Gomes, H.D.R.; Chekalyuk, A.M.; Carpenter, E.J.; Montoya, J.P.; Coles, V.J.; Yager, P.L.; Berelson, W.M.; Capone, D.G.; Foster, R. a.; et al. Influence of the Amazon River Discharge on the Biogeography of Phytoplankton Communities in the Western Tropical North Atlantic. *Prog. Oceanogr.* **2014**, *120*, 29–40. https://doi.org/10.1016/j.pocean.2013.07.010.
8. Grodsky, S. a.; Reverdin, G.; Carton, J. a.; Coles, V.J. Year-to-Year Salinity Changes in the Amazon Plume: Contrasting 2011 and 2012 Aquarius/SACD and SMOS Satellite Data. *Remote Sens. Environ.* **2014**, *140*, 14–22. https://doi.org/10.1016/j.rse.2013.08.033.

9. Coles, V.J.; Brooks, M.T.; Hopkins, J.; Stukel, M.R.; Yager, P.L.; Hood, R.R. The Pathways and Properties of the Amazon River Plume in the Tropical North Atlantic Ocean. *J. Geophys. Res. Ocean.* **2013**, *118*, 6894–6913. https://doi.org/10.1002/2013JC008981.
10. Molleri, G.S.F.; Novo, E.M.L. d. M.L.D.M.; Kampel, M. Space-Time Variability of the Amazon River Plume Based on Satellite Ocean Color. *Cont. Shelf Res.* **2010**, *30*, 342–352. https://doi.org/10.1016/j.csr.2009.11.015.
11. Subramaniam, A.; Yager, P.L.; Carpenter, E.J.; Mahaffey, C.; Björkman, K.; Cooley, S.; Kustka, A.B.; Montoya, J.P.; Sañudo-Wilhelmy, S.A.; Shipe, R.; et al. Amazon River Enhances Diazotrophy and Carbon Sequestration in the Tropical North Atlantic Ocean. *Proc. Natl. Acad. Sci. USA* **2008**, *105*, 10460–10465. https://doi.org/10.1073/pnas.0710279105.
12. Cooley, S.R.; Coles, V.J.; Subramaniam, A.; Yager, P.L. Seasonal Variations in the Amazon Plume-Related Atmospheric Carbon Sink. *Glob. Biogeochem. Cycles* **2007**, *21*, 1–15. https://doi.org/10.1029/2006GB002831.
13. Tyler, A.N.; Hunter, P.D.; Spyrakos, E.; Groom, S.; Constantinescu, A.M.; Kitchen, J. Developments in Earth Observation for the Assessment and Monitoring of Inland, Transitional, Coastal and Shelf-Sea Waters. *Sci. Total Environ.* **2016**, *572*, 1307–1321. https://doi.org/10.1016/j.scitotenv.2016.01.020.
14. Palmer, S.C.J.; Kutser, T.; Hunter, P.D. Remote Sensing of Inland Waters : Challenges , Progress and Future Directions. *Remote Sens. Environ.* **2015**, *157*, 1–8. https://doi.org/10.1016/j.rse.2014.09.021.
15. IOCCG. *Atmospheric Correction for Remotely-Sensed Ocean-Colour Products*; Wang, M., Ed.; International Ocean Colour Coordinating Group (IOCCG): Dartmouth, NS, Canada, 2010; ISBN 9781896246611.
16. Shi, W.; Wang, M. An Assessment of the Black Ocean Pixel Assumption for MODIS SWIR Bands. *Remote Sens. Environ.* **2009**, *113*, 1587–1597. https://doi.org/10.1016/j.rse.2009.03.011.
17. Loisel, H.; Vantrepotte, V.; Jamet, C.; Dat, D.N. Challenges and New Advances in Ocean Color Remote Sensing of Coastal Waters. In *Topics in Oceanography*; IntechOpen Limited: London, UK, 2013; pp. 1–38.
18. Shanmugam, P. CAAS: An Atmospheric Correction Algorithm for the Remote Sensing of Complex Waters. *Ann. Geophys.* **2012**, *30*, 203–220. https://doi.org/10.5194/angeo-30-203-2012.
19. Wang, M.; Shi, W. The NIR-SWIR Combined Atmospheric Correction Approach for MODIS Ocean Color Data Processing. *Opt. Express* **2007**, *15*, 15722–15733. https://doi.org/10.1029/2004JD004950.
20. Ruddick, K.G.; Ovidio, F.; Rijkeboer, M. Atmospheric Correction of SeaWiFS Imagery for Turbid Coastal and Inland Waters. *Appl. Opt.* **2000**, *39*, 897–912.
21. Vanhellemont, Q.; Ruddick, K. Advantages of High Quality SWIR Bands for Ocean Colour Processing: Examples from Landsat-8. *Remote Sens. Environ.* **2015**, *161*, 89–106. https://doi.org/10.1016/j.rse.2015.02.007.
22. Gitelson, A.A.; Dall'Olmo, G.; Moses, W.; Rundquist, D.C.; Barrow, T.; Fisher, T.R.; Gurlin, D.; Holz, J. A Simple Semi-Analytical Model for Remote Estimation of Chlorophyll-a in Turbid Waters: Validation. *Remote Sens. Environ.* **2008**, *112*, 3582–3593.
23. Valerio, A.D.M.; Kampel, M.; Vantrepotte, V.; Ward, N.D.; Richey, J.E. Optical Classification of Lower Amazon Waters Based on In Situ Data and Sentinel-3 Ocean and Land Color Instrument Imagery. *Remote Sens.* **2021**, *13*, 3057. https://doi.org/10.3390/rs13163057.
24. Aurin, D.A.; Dierssen, H.M. Advantages and Limitations of Ocean Color Remote Sensing in CDOM-Dominated, Mineral-Rich Coastal and Estuarine Waters. *Remote Sens. Environ.* **2012**, *125*, 181–197. https://doi.org/10.1016/j.rse.2012.07.001.
25. Matthews, M.W. A Current Review of Empirical Procedures of Remote Sensing in Inland and Near-Coastal Transitional Waters. *Int. J. Remote Sens.* **2011**, *32*, 6855–6899. https://doi.org/10.1080/01431161.2010.512947.
26. Siegel, D.A.; Wang, M.; Robinson, W. Atmospheric Correction of Satellite Ocean Color Imagery: The Black Pixel Assumption. *Appl. Opt.* **2000**, *39*, 3582–3591.
27. Pahlevan, N.; Mangin, A.; Balasubramanian, S.V.; Smith, B.; Alikas, K.; Arai, K.; Barbosa, C.; Bélanger, S.; Binding, C.; Bresciani, M.; et al. ACIX-Aqua: A Global Assessment of Atmospheric Correction Methods for Landsat-8 and Sentinel-2 over Lakes, Rivers, and Coastal Waters. *Remote Sens. Environ.* **2021**, *258*. https://doi.org/10.1016/j.rse.2021.112366.
28. Kuhn, C.; Valerio, A. de M.; Ward, N.; Loken, L.; Sawakuchi, H.; Kampel, M.; Richey, J.; Stadler, P.; Crawford, J.; Striegl, R.; et al. Performance of Landsat-8 and Sentinel-2 Surface Reflectance Products for River Remote Sensing Retrievals of Chlorophyll-a and Turbidity. *Remote Sens. Environ.* **2019**, *224*, 104–118. https://doi.org/10.1016/j.rse.2019.01.023.
29. Martins, V.S.; Barbosa, C.C.F.; de Carvalho, L.A.S.; Jorge, D.S.F.; Lobo, F. de L.; de Moraes Novo, E.M.L. Assessment of Atmospheric Correction Methods for Sentinel-2 MSI Images Applied to Amazon Floodplain Lakes. *Remote Sens.* **2017**, *9*, 322. https://doi.org/10.3390/rs9040322.
30. Mograne, M.A.; Jamet, C.; Loisel, H.; Vantrepotte, V.; Mériaux, X.; Cauvin, A. Evaluation of Five Atmospheric Correction Algorithms over French Optically-Complex Waters for the Sentinel-3a Olci Ocean Color Sensor. *Remote Sens.* **2019**, *11*, 668. https://doi.org/10.3390/RS11060668.
31. Dierssen, H.M.; Vandermeulen, R.A.; Barnes, B.B.; Castagna, A.; Knaeps, E.; Vanhellemont, Q. QWIP: A Quantitative Metric for Quality Control of Aquatic Reflectance Spectral Shape Using the Apparent Visible Wavelength. *Front. Remote Sens.* **2022**, *3*, 869611. https://doi.org/10.3389/frsen.2022.869611.
32. Turner, K.J.; Tzortziou, M.; Grunert, B.K.; Goes, J.; Sherman, J. Optical Classification of an Urbanized Estuary Using Hyperspectral Remote Sensing Reflectance. *Opt. Express* **2022**, *30*, 41590. https://doi.org/10.1364/oe.472765.
33. Sawakuchi, H.O.; Neu, V.; Ward, N.D.; Barros, M.D.L.C.; Valerio, A.; Gagne-maynard, W.; Cunha, A.C.; Fernanda, D.; Diniz, J.E.; Brito, D.C.; et al. Carbon Dioxide Emissions along the Lower Amazon River. *Front. Mar. Sci.* **2017**, *4*, 76. https://doi.org/10.3389/fmars.2017.00076.

34. Gouveia, N.A.; Gherardi, D.F.M.; Wagner, F.H.; Paes, E.T.; Coles, V.J.; Aragão, L.E.O.C. The Salinity Structure of the Amazon River Plume Drives Spatiotemporal Variation of Oceanic Primary Productivity. *J. Geophys. Res. Biogeosci.* **2019**, *124*, 147–165. https://doi.org/10.1029/2018JG004665.
35. Masson, S.; Delecluse, P. Influence of the Amazon River Runoff on the Tropical Atlantic. *Phys. Chem. Earth Part B Hydrol. Ocean. Atmos.* **2001**, *26*, 137–142. https://doi.org/10.1016/S1464-1909(00)00230-6.
36. Lentz, S.J.; Limeburner, R. The Amazon River Plume during AMASSEDS: Spatial Characteristics and Salinity Variability. *J. Geophys. Res.* **1995**, *100*, 2355–2375. https://doi.org/10.1029/94JC01411.
37. Mobley, C.D. Estimation of the Remote-Sensing Reflectance from above-Surface Measurements. *Appl. Opt.* **1999**, *38*, 7442–7455.
38. Ruddick, K.G.; Cauwer, V. De; Park, Y.; Moore, G. Seaborne Measurements of near Infrared Water-Leaving Reflectance: The Similarity Spectrum for Turbid Waters. *Limnol. Ocean.* **2006**, *51*, 1167–1179.
39. Pitarch, J.; Talone, M.; Zibordi, G.; Groetsch, P. Determination of the Remote-Sensing Reflectance from above-Water Measurements with the "3C Model": A Further Assessment. *Opt. Express* **2020**, *28*, 15885. https://doi.org/10.1364/oe.388683.
40. Mélin, F.; Vantrepotte, V. How Optically Diverse Is the Coastal Ocean? *Remote Sens. Environ.* **2015**, *160*, 235–251. https://doi.org/10.1016/j.rse.2015.01.023.
41. Vantrepotte, V.; Loisel, H.; Dessailly, D.; Mériaux, X. Optical Classification of Contrasted Coastal Waters. *Remote Sens. Environ.* **2012**, *123*, 306–323. https://doi.org/10.1016/j.rse.2012.03.004.
42. Schowengerdt, R.A. *Remote Sensing: Models and Methods for Image Processing*, 2nd ed.; Elsevier: Amsterdam, The Netherlands, 2012; ISBN 9780080516103.
43. Müller, D.; Krasemann, H.; Brewin, R.J.W.; Brockmann, C.; Deschamps, P.Y.; Doerffer, R.; Fomferra, N.; Franz, B.A.; Grant, M.G.; Groom, S.B.; et al. The Ocean Colour Climate Change Initiative: I. A Methodology for Assessing Atmospheric Correction Processors Based on In-Situ Measurements. *Remote Sens. Environ.* **2015**, *162*, 242–256. https://doi.org/10.1016/j.rse.2013.11.026.
44. Bailey, S.W.; Werdell, P.J. A Multi-Sensor Approach for the on-Orbit Validation of Ocean Color Satellite Data Products. *Remote Sens. Environ.* **2006**, *102*, 12–23. https://doi.org/10.1016/j.rse.2006.01.015.
45. Vanhellemont, Q.; Ruddick, K. Acolite for Sentinel-2: Aquatic Applications of MSI Imagery. In Proceedings of the 2016 ESA Living Planet Symposium, Prague, Czech Republic, 9–13 May 2016; (Special Publication) ESA SP; European Space Agency: Paris, France, 2016.
46. Vanhellemont, Q.; Ruddick, K. Atmospheric Correction of Metre-Scale Optical Satellite Data for Inland and Coastal Water Applications. *Remote Sens. Environ.* **2018**, *216*, 586–597. https://doi.org/10.1016/j.rse.2018.07.015.
47. Vanhellemont, Q. Adaptation of the Dark Spectrum Fitting Atmospheric Correction for Aquatic Applications of the Landsat and Sentinel-2 Archives. *Remote Sens. Environ.* **2019**, *225*, 175–192. https://doi.org/10.1016/j.rse.2019.03.010.
48. Steinmetz, F.; Deschamps, P.-Y.; Ramon, D. (POLYMER)Atmospheric Correction in Presence of Sun Glint: Application to MERIS. *Opt. Express* **2011**, *19*, 9783–9800. https://doi.org/10.1364/OE.19.009783.
49. Doerffer, R.; Schiller, H. The MERIS Case 2 Water Algorithm. *Int. J. Remote Sens.* **2007**, *28*, 517–535. https://doi.org/10.1080/01431160600821127.
50. Fan, Y.; Li, W.; Chen, N.; Ahn, J.H.; Park, Y.J.; Kratzer, S.; Schroeder, T.; Ishizaka, J.; Chang, R.; Stamnes, K. OC-SMART: A Machine Learning Based Data Analysis Platform for Satellite Ocean Color Sensors. *Remote Sens. Environ.* **2021**, *253*, 112236. https://doi.org/10.1016/j.rse.2020.112236.
51. Vandermeulen, R.A.; Mannino, A.; Craig, S.E.; Werdell, P.J. 150 Shades of Green: Using the Full Spectrum of Remote Sensing Reflectance to Elucidate Color Shifts in the Ocean. *Remote Sens. Environ.* **2020**, *247*, 111900. https://doi.org/10.1016/j.rse.2020.111900.
52. Tran, M.D.; Vantrepotte, V.; Loisel, H.; Oliveira, E.N.; Tran, K.T.; Jorge, D.; Mériaux, X.; Paranhos, R. Band Ratios Combination for Estimating Chlorophyll-a from Sentinel-2 and Sentinel-3 in Coastal Waters. *Remote Sens.* **2023**, *15*, 1653. https://doi.org/10.3390/rs15061653.
53. Liu, H.; He, X.; Li, Q.; Hu, X.; Ishizaka, J.; Kratzer, S.; Yang, C.; Shi, T.; Hu, S.; Zhou, Q.; et al. Evaluation of Ocean Color Atmospheric Correction Methods for Sentinel-3 OLCI Using Global Automatic In Situ Observations. *IEEE Trans. Geosci. Remote Sens.* **2022**, *60*, 4206319. https://doi.org/10.1109/TGRS.2021.3136243.
54. Nittrouer, C.A.; DeMaster, D.J.; Kuehl, S.A.; Figueiredo, A.G.; Sternberg, R.W.; Faria, L.E.C.; Silveira, O.M.; Allison, M.A.; Kineke, G.C.; Ogston, A.S.; et al. Amazon Sediment Transport and Accumulation Along the Continuum of Mixed Fluvial and Marine Processes. *Ann. Rev. Mar. Sci.* **2021**, *13*, 501–536. https://doi.org/10.1146/annurev-marine-010816-060457.
55. Spyrakos, E.; O'Donnell, R.; Hunter, P.D.; Miller, C.; Scott, M.; Simis, S.G.H.; Neil, C.; Barbosa, C.C.F.; Binding, C.E.; Bradt, S.; et al. Optical Types of Inland and Coastal Waters. *Limnol. Oceanogr.* **2018**, *63*, 846–870. https://doi.org/10.1002/lno.10674.
56. Brockmann, C.; Doerffer, R.; Peters, M.; Stelzer, K.; Embacher, S.; Ruescas, A. Evolution of the C2RCC Neural Network for Sentinel 2 and 3 for the Retrieval of Ocean Colour Products in Normal and Extreme Optically Complex Waters. In Proceedings of the European Space Agency, (Special Publication) ESA SP, Prague, Czech Republic, held 9–13 May 2016; Volume SP-740, p. 54.
57. Renosh, P.R.; Doxaran, D.; De Keukelaere, L.; Gossn, J.I. Evaluation of Atmospheric Correction Algorithms for Sentinel-2-MSI and Sentinel-3-OLCI in Highly Turbid Estuarine Waters. *Remote Sens.* **2020**, *12*, 1285. https://doi.org/10.3390/RS12081285.
58. Lehmann, M.K.; Gurlin, D.; Pahlevan, N.; Alikas, K.; Anstee, J.; Balasubramanian, S.V.; Barbosa, C.C.F.; Binding, C.; Bracher, A.; Bresciani, M.; et al. GLORIA—A Globally Representative Hyperspectral In Situ Dataset for Optical Sensing of Water Quality. *Sci. Data* **2023**, *10*, 100. https://doi.org/10.1038/s41597-023-01973-y.

59. Hieronymi, M.; Bi, S.; Müller, D.; Schütt, E.M.; Behr, D.; Brockmann, C.; Lebreton, C.; Steinmetz, F.; Stelzer, K.; Vanhellemont, Q. Ocean Color Atmospheric Correction Methods in View of Usability for Different Optical Water Types. *Front. Mar. Sci.* **2023**, *10*, 1129876. https://doi.org/10.3389/fmars.2023.1129876.
60. Zorrilla, N.A.; Vantrepotte, V.; Ngoc, D.D.; Huybrechts, N.; Gardel, A. Automated SWIR Based Empirical Sun Glint Correction of Landsat 8-OLI Data over Coastal Turbid Water. *Opt. Express* **2019**, *27*, A294. https://doi.org/10.1364/oe.27.00a294.